

Spherical Convolutional Neural Networks: Stability to Perturbations in $SO(3)$

Zhan Gao[†], Fernando Gama[‡] and Alejandro Ribeiro[†]

Abstract

Spherical convolutional neural networks (Spherical CNNs) learn nonlinear representations from 3D data by exploiting the data structure and have shown promising performance in shape analysis, object classification, and planning among others. This paper investigates the properties that Spherical CNNs exhibit as they pertain to the rotational structure inherent in spherical signals. We build upon the rotation equivariance of spherical convolutions to show that Spherical CNNs are stable to general structure perturbations. In particular, we model arbitrary structure perturbations as diffeomorphism perturbations, and define the rotation distance that measures how far from rotations these perturbations are. We prove that the output change of a Spherical CNN induced by the diffeomorphism perturbation is bounded proportionally by the perturbation size under the rotation distance. This stability property coupled with the rotation equivariance provide theoretical guarantees that underpin the practical observations that Spherical CNNs exploit the rotational structure, maintain performance under structure perturbations that are close to rotations, and offer good generalization and faster learning.

Keywords: Spherical convolutional neural networks, spherical convolutional filters, structure perturbations, stability analysis

[†]Department of Electrical and Systems Engineering, University of Pennsylvania, USA. Email: {gaozhan,aribeiro}@seas.upenn.edu. [‡]Department of Electrical Engineering and Computer Sciences, University of California, Berkeley, USA. Email: fgama@berkeley.edu

1. Introduction

Modern image-acquisition technologies such as light detection and ranging (LIDAR) [1], panorama cameras [2] and optical scanners [3] obtain data that can be modelled on the spherical surface in 3D space [4]. Spherical signals offer mathematical representations for such data, which essentially assign a scalar (or vector) value to each point on the spherical surface [5, 6], and have been leveraged in applications of object classification in computer vision [7], panoramic video processing in self-driving cars [8] and 3D surface reconstruction in medical imaging [9]. Processing spherical signals in a successful manner entails architectures capable of exploiting the structural information given by the spherical surface. In particular, we are concerned about exploiting the rotational structure inherent in spherical signals [10, 11].

The rotational structure can be captured by means of the rotation group. This is a mathematical group defined in the space of spherical surface equipped with the operation of rotation [12]. The rotation group admits the definition of convolution operation for spherical signals, which in turn gives rise to spherical convolutional filters [13]. The latter are linear processing operators that compute weighted, rotated linear combinations of spherical signal values [14, 15]. Spherical convolutional filters exhibit the property of rotation equivariance, which means that they yield the same features irrespective of rotated versions of the input spherical signal [16, 17]. This property is particularly meaningful when processing 3D data where the information is contained in the relative location of signal values but not their absolute positions [18, 19, 20]. Therefore, processing spherical signals with spherical convolutional filters, allows the resulting architecture to exploit the data structure for information extraction.

Spherical convolutional neural networks (Spherical CNNs) are developed as nonlinear processing architectures that consist of a cascade of layers, each of which applies a spherical convolutional filter followed by a pointwise nonlinearity [16, 17, 21, 22, 23, 24]. The inclusion of nonlinearities coupled with the cascade of multiple layers dons Spherical CNNs with an enhanced representa-

tive power, thus exhibiting superior performance for spherical signal processing. Several Spherical CNN architectures have been proposed, leveraging different implementations of the spherical convolution. In particular, [16, 17] carry out the spherical convolution through the spherical harmonic transform, while [21, 22, 23, 24] discretize the sphere using a graph connecting pixels and then approximate the spherical convolution with the Laplacian-based graph convolution.

Considering the evident success of Spherical CNNs in 3D tasks, we focus on analyzing the properties that Spherical CNNs exhibit as they pertain to the rotational structure present in spherical signals. These properties are meant to shed light on the reasons behind this observed success and provide theoretical guarantees on the performance robustness under structure perturbations. Rotation equivariance of spherical convolutional linear filters was established in [16, 17], and Spherical CNNs were shown to be numerically effective in standard retrieval and classification problems.

In this paper, we further investigate how spherical convolutional filters and Spherical CNNs react to general structure perturbations applied on input spherical signals. More specifically, we build upon the rotation equivariance of spherical convolutions [16, 17] to prove that Spherical CNNs are Lipschitz stable to structure perturbations. To conduct such analysis, we leverage the Euler parametrization together with the normalized Haar measure to carry out spherical convolutions explicitly in the spherical coordinate system. We also model the arbitrary structure perturbation as the diffeomorphism perturbation, and define a notion of rotation distance that measures the difference between diffeomorphism perturbations and rotation operations. The established stability results indicate that Spherical CNNs extract the same information under rotations, and more importantly, it is able to maintain performance when structure perturbations are close to rotations. Our detailed contributions can be summarized as follows.

- (i) *Stability of spherical convolutional filters (Section 3)*: We prove the out-

put difference of spherical convolutional filters induced by general structure perturbations, defined as diffeomorphism perturbations, is bounded proportionally by the perturbation size under the rotation distance [Thm. 1]. This result extends the stability analysis from regular rotation operations to irregular diffeomorphism perturbations, and establishes that almost same information can be extracted if structure perturbations are close to rotation operations.

- (ii) *Stability of Spherical CNNs (Section 4)*: We show Spherical CNNs inherit the stability to general structure perturbations with a factor proportional to the perturbation size [Thm. 2]. It also indicates the explicit impact of the filter, the nonlinearity, the architecture width and depth on the stability property. In particular, a wider and deeper Spherical CNN degrades the stability but improves the representative power, indicating a trade-off between these two factors.

The stability property to arbitrary perturbations plays an important role in improving the generalization capability of Spherical CNNs. In the case of 3D object identification [25], for instance, mild changes in spherical signals may be introduced by different viewing angles or distances but Spherical CNNs are expected to extract the same information. Section 5 provides numerical experiments to corroborate theory on the problem of 3D object classification and Section 6 concludes the paper. All proofs are collected in the appendix.

2. Spherical Convolutional Neural Networks

Signals arising from 3D data, e.g., LIDAR images, X-ray models, surface data, etc., can be described as inscribed on the spherical surface in 3D space [5, 6]. In Sec. 2.1 we introduce the mathematical description of these spherical signals, in Sec. 2.3 we discuss the spherical convolution as the fundamental linear operation between spherical signals, and in Sec. 2.4 we present the spherical convolutional neural network (Spherical CNN).

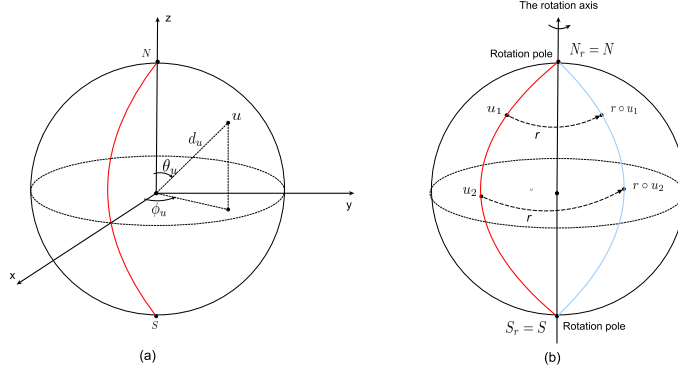


Figure 1. (a) The spherical coordinate system. (b) Azimuthal rotation on the sphere. The rotation displaces points on the sphere along the rotation axis, e.g., it displaces points on the red line to corresponding points on the blue line.

2.1. Spherical signal

Let $\mathbb{S}_2 \subset \mathbb{R}^3$ be the spherical surface contained in \mathbb{R}^3 . Given a coordinate system $\mathcal{S}(x, y, z)$, a point $u = (x_u, y_u, z_u) \in \mathbb{S}_2$ can be alternatively described by the polar angle $\theta_u = \arctan(\sqrt{x_u^2 + y_u^2}/z_u) \in [0, \pi]$ from the z -direction, the azimuth angle $\phi_u = \arctan(x_u/y_u) \in [0, 2\pi)$ along the xy -plane, and the distance $d = \sqrt{x_u^2 + y_u^2 + z_u^2}$ from the origin. Without loss of generality, we assume the unit sphere with $d = 1$ —see Fig. 1a for the spherical coordinate system. More specifically, a point $u \in \mathbb{S}_2$ can be represented by the vector

$$u = (\theta_u, \phi_u) = [\sin(\theta_u) \cos(\phi_u), \sin(\theta_u) \sin(\phi_u), \cos(\theta_u)]. \quad (1)$$

For points whose polar angle are $\theta_u = 0$ or $\theta_u = \pi$, the azimuth angle is assumed to be zero. These points are known as the north and south poles, referred to as $N \in \mathbb{S}_2$ and $S \in \mathbb{S}_2$ respectively [cf. Fig. 1a].

A *spherical signal* is defined as the map $x : \mathbb{S}_2 \rightarrow \mathbb{R}$ which assigns a scalar $x(u) \in \mathbb{R}$ to each point $u \in \mathbb{S}_2$ on the sphere. Equivalently, these signals can be represented as mappings from the pair of angular variables (θ_u, ϕ_u) to the real line \mathbb{R} , i.e. $x(u) = x(\theta_u, \phi_u) \in \mathbb{R}$. Spherical signals are typically used to describe data collected from 3D objects—see Fig. 2 for an example on how to cast the surface of 3D objects as spherical signals.

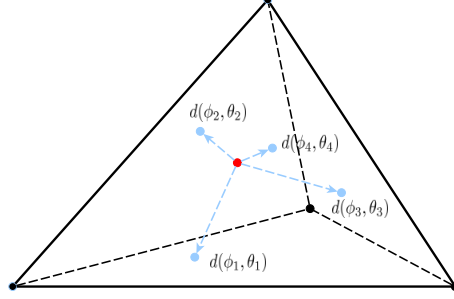


Figure 2. Spherical signal representing the surface data of a tetrahedron. The tetrahedron contains interior points from which the whole boundary is visible. Assume the object center as one of these interior points, from which we cast rays that intersect the object surface. Denote by $d(\phi_u, \theta_u)$ the distance between the farthest intersection point and the center along the ray direction (ϕ_u, θ_u) , where θ_u is the polar angle and ϕ_u is the azimuth angle. The surface data can be represented as a spherical signal $x(\phi_u, \theta_u) = d(\phi_u, \theta_u) \in \mathbb{R}$, which maps angular variables to the distance.

2.2. Rotation operation

Rotations are elementary operations to which a spherical signal can be subject [10, 11]. A *rotation* r is uniquely characterized by the rotation point $N^r \in \mathbb{S}_2$ and the rotation angle $\beta^r \in [0, 2\pi)$. It displaces the points on the sphere by β^r degrees along the axis that passes through the origin and the point N^r ; thus, we may refer to N^r as the rotation axis. To describe the rotation in the spherical coordinate system [cf. (1)], let $r^\theta : \mathbb{S}_2 \rightarrow \mathbb{R}$ be the polar angle displacement and $r^\phi : \mathbb{S}_2 \rightarrow \mathbb{R}$ be the azimuth angle displacement induced by the rotation r . These two quantities parametrize the rotation operation $r : \mathbb{S}_2 \rightarrow \mathbb{S}_2$ as

$$r(u) = r(\theta_u, \phi_u) = [\sin(\theta_u + r^\theta(\theta_u, \phi_u)) \cos(\phi_u + r^\phi(\theta_u, \phi_u)), \quad (2) \\ \sin(\theta_u + r^\theta(\theta_u, \phi_u)) \sin(\phi_u + r^\phi(\theta_u, \phi_u)), \cos(\theta_u + r^\theta(\theta_u, \phi_u))]$$

where r^θ and r^ϕ are determined by the Rodrigues' rotation formula [26]. The rotation operation takes a point u on the sphere \mathbb{S}_2 and maps it into another point $r(u)$, also on the sphere \mathbb{S}_2 , but where the polar angle has been displaced by r^θ and the azimuthal angle by r^ϕ . The rotation axis intersects the spher-

ical surface at two points, namely $N^r \in \mathbb{S}_2$ referred to as the rotation north pole and $S^r \in \mathbb{S}_2$ referred to as the rotation south pole. These two points remain unchanged under the rotation operation. As an illustrative example, consider the azimuthal rotation whose rotation axis coincides with the z -axis of the coordinate system $\mathcal{S}(x, y, z)$, i.e. $N^r = N$ and $S^r = S$ —see Fig. 1b. Then, $r^\theta(\theta_u, \phi_u) = 0$ and $r^\phi(\theta_u, \phi_u) = \beta^r$ are constants for all $(\theta_u, \phi_u) \in [0, \pi] \times [0, 2\pi)$.

We can also describe the rotation operation $r \in \text{SO}(3)$ in terms of the ZYZ Euler parametrization as

$$r = r_{\phi_r \theta_r \rho_r} = r_{\phi_r}^z \circ r_{\theta_r}^y \circ r_{\rho_r}^z \quad (3)$$

where $r_{\phi_r}^z$, $r_{\theta_r}^y$ and $r_{\rho_r}^z$ are the rotations along the Euclidean coordinate axes with the rotation angles of $\phi_r \in [0, 2\pi)$, $\theta_r \in [0, \pi]$ and $\rho_r \in [0, 2\pi)$, respectively. The Euler parametrization allows us to decompose any rotation r as three consecutive rotations. The set of all rotation operations about the origin [cf. (2)] defines a mathematical group under the operation of composition, referred to as the *3D rotation group* $\text{SO}(3)$ [27, 28]. This is a group in the sense that (i) composing two rotations $r_1, r_2 \in \text{SO}(3)$ results in another rotation $r_1 \circ r_2 \in \text{SO}(3)$, (ii) rotations are associative $(r_1 \circ r_2) \circ r_3 = r_1 \circ (r_2 \circ r_3)$ for any $r_1, r_2, r_3 \in \text{SO}(3)$, (iii) the rotation determined by $r^\theta = r^\phi = 0$ is the identity rotation $r_0 \in \text{SO}(3)$ such that $r \circ r_0 = r$ for all $r \in \text{SO}(3)$, and (iv) for every rotation $r \in \text{SO}(3)$ there exists another rotation $r^{-1} \in \text{SO}(3)$, such that $r \circ r^{-1} = r_0$.

2.3. Spherical convolution

The spherical surface \mathbb{S}_2 is now equipped with the rotation operation that conforms a mathematical group. This allows defining the convolution operation for spherical signals. Given two signals $x, h : \mathbb{S}_2 \rightarrow \mathbb{R}$ the spherical convolution $*_{\text{SO}(3)}$ between them is defined as

$$y(u) = (h *_{\text{SO}(3)} x)(u) = \int_{\text{SO}(3)} h(r^{-1}(u))x(r(u_0)) \, dr, \quad \forall u \in \mathbb{S}_2 \quad (4)$$

where $y(u)$ is the output spherical signal and $u_0 = (0, 0) \in \mathbb{S}_2$ is the point given by $\theta_{u_0} = \phi_{u_0} = 0$.

We can rewrite the convolution operation in the spherical coordinate system by leveraging the Euler parametrization of rotations [cf. (3)]. Recall the normalized Haar measure on the rotation group $\text{SO}(3)$ as [29]

$$dr = \frac{d\phi_r}{2\pi} \frac{\sin(\theta_r)d\theta_r}{2} \frac{d\rho_r}{2\pi}, \quad (5)$$

and we can rewrite (4) as

$$\begin{aligned} y(u) &= (h *_{\text{SO}(3)} x)(u) \\ &= \frac{1}{8\pi^2} \int h(r_{\phi_r, \theta_r, \rho_r}^{-1}(u)) x(r_{\phi_r, \theta_r, \rho_r}(u_0)) \sin(\theta_r) d\theta_r d\phi_r d\rho_r \end{aligned} \quad (6)$$

where $r_{\phi_r, \theta_r, \rho_r}$ is the rotation parametrized by Euler angles ϕ_r, θ_r, ρ_r [cf. (3)] and $r_{\phi_r, \theta_r, \rho_r}^{-1}$ is its inverse rotation. In the spherical coordinate system, by noting that $r_{\phi_r, \theta_r, \rho_r}(u_0) = (\theta_r, \phi_r)$ and using the Rodrigues' formula (2), we further get

$$\begin{aligned} y(\theta_u, \phi_u) &= (h *_{\text{SO}(3)} x)(\theta_u, \phi_u) \\ &= \frac{1}{8\pi^2} \int h(\theta_u + r_{\phi_r, \theta_r, \rho_r}^{\theta-1}(\theta_u, \phi_u), \phi_u + r_{\phi_r, \theta_r, \rho_r}^{\phi-1}(\theta_u, \phi_u)) x(\theta_r, \phi_r) \sin(\theta_r) d\theta_r d\phi_r d\rho_r. \end{aligned} \quad (7)$$

where $r_{\phi_r, \theta_r, \rho_r}^{\theta-1}$ and $r_{\phi_r, \theta_r, \rho_r}^{\phi-1}$ are angle displacements induced by $r_{\phi_r, \theta_r, \rho_r}^{-1}$. We see that (7) is equivalent to (4) and (6), but described in terms of the polar angle θ_u and the azimuthal angle ϕ_u on which we can evaluate the output of spherical convolution mathematically. That is, we move from a description given entirely in the realm of rotation group $\text{SO}(3)$ to a description given by specific angular variables in the spherical coordinate system [cf. (1)]. It is important because this allows us to carry out the integral of the spherical convolution explicitly, serving for the stability analysis in the following sections.

Remark 1 (Group convolution). Convolution operations can be formally defined with respect to any group that is applicable to the space on which the convolving signals are defined. That is, let $x, h : \mathbb{X} \rightarrow \mathbb{R}$ be two signals mapping some space \mathbb{X} into the real line, and let $\mathbf{G} = \mathbf{G}(\mathbb{X}, \circ)$ be a group where the element $g \in \mathbf{G}$ is defined over \mathbb{X} , \circ is the binary operation, and $g^{-1} \in \mathbf{G}$ is the inverse element. The convolution operation $*_{\mathbf{G}}$ is generically defined as

$$(h *_{\mathbf{G}} g)(u) = \int_{\mathbf{G}} h(g^{-1}(u)) x(g(u_0)) dg \quad (8)$$

with $u, u_0 \in \mathbb{X}$. The spherical convolution (4) is one instance of the group convolution for $G = \text{SO}(3)$. Another example is the regular convolution defined over the group of translations. We remark that many of the results derived in this work are applicable to generic group convolutions—see [30] for details.

2.4. Spherical convolutional neural network

Spherical convolutions are linear operations that exploit the rotational structure present in spherical signals. Thus, they can be used to regularize the linear transform in neural networks such that the resulting architecture is able to leverage the rotational structure when processing spherical signals from 3-D tasks. In particular, neural networks are nonlinear maps that consist of a cascade of L layers, each applying a linear transform A_ℓ followed by a pointwise nonlinearity σ_ℓ [31, Ch. 6]

$$x_\ell = \sigma_\ell \left[A_\ell x_{\ell-1} \right], \ell = 1, \dots, L \quad (9)$$

with $x_0 = x$ the input signal. The number of layers L as well as the specific form of nonlinearity σ_ℓ are typically design choices, while the linear transforms $\{A_\ell\}_{\ell=1}^L$ are *learned* by minimizing some objective function over a training set. Neural networks in such a general form work well only for small input data size, otherwise the space of learnable linear transforms $\{A_\ell\}_{\ell=1}^L$ becomes too large to efficiently explore, and the resulting mapping rarely generalizes well [31, Ch. 9]. Successful neural network architectures like convolutional neural networks [32, 33, 34] or graph neural networks [35, 36, 37] typically regularize the space of linear transforms by imposing the data structure information on the operation A_ℓ (e.g., CNNs exploit the Euclidean structure present in data and GNNs exploit the graph structure present in data).

Working with spherical signals demands neural network architectures that exploit the rotational structure. This motivates to develop the spherical convolutional neural network (Spherical CNN) where we regularize the linear transform A_ℓ to be a spherical convolution [cf. (4)], namely

$$x_\ell = \sigma_\ell \left[h_\ell *_{\text{SO}(3)} x_{\ell-1} \right], \ell = 1, \dots, L \quad (10)$$

with $x_0 = x$ the input signal [16]. We see in (10) that the linear transform is now forced to be a spherical convolution. The learnable linear transforms are now the collection of spherical convolutional filters $\mathcal{H} = \{h_\ell\}_{\ell=1}^L$.

The descriptive power of Spherical CNNs can be enhanced by considering a multi-feature signal mapping $\mathbf{x} : \mathbb{S}_2 \rightarrow \mathbb{R}^F$, where we map each point on the sphere to a F -dimensional vector. Each entry of the vector is termed a *feature* and the multi-feature spherical signal can be thought of as a collection of F single-feature spherical signals $x^f : \mathbb{S}_2 \rightarrow \mathbb{R}$, i.e. $\mathbf{x} = \{x^f\}_{f=1}^F$. In this context, the convolution operation becomes a series of spherical convolutions where the input signal is processed through a filter bank. More specifically, an output signal with G features $\mathbf{y} : \mathbb{S}^2 \rightarrow \mathbb{R}^G$ can be obtained by

$$y^g = \sum_{f=1}^F h^{fg} *_{\text{SO}(3)} x^f, \quad \forall f = 1, \dots, F, \quad g = 1, \dots, G. \quad (11)$$

Operations (11) define the spherical convolution acting on multi-feature spherical signals, which is equivalent to filtering F features of the input signal through a bank of FG filters and then aggregating the output of each g th filter across all F input features. To simplify notation, we denote the single-feature spherical convolution [cf. (4)] as a filtering operation, i.e. $y = H(x) = h *_{\text{SO}(3)} x$. The output of the last layer is $\Phi(x; \mathcal{H}) = x_L$ where $\Phi : \mathbb{S}_2 \rightarrow \mathbb{S}_2$ represents the nonlinear mapping given by the Spherical CNN [cf. (10)]. The learnable parameters in the Spherical CNN consist of the filters $\mathcal{H} = \{H_\ell\}_{\ell=1}^L$ (or $\mathcal{H} = \{H_\ell^{fg}\}_{\ell=1}^L$ for the multi-feature scenario). The design hyperparameters are the number of layers L , the nonlinearity σ_ℓ , and the number of features F_ℓ at each layer.

The resulting Spherical CNN [cf. (10)] leverages the 3D data structure and thus, we expect it to exhibit strong performance on 3D tasks (as a matter of fact, this is observed in practice [16]). In what follows, we aim to analyze the properties that Spherical CNNs exhibit when processing spherical signals, i.e., the stability to arbitrary structure perturbations, to explicitly illustrate how they exploit the rotational structure and to bring insights behind their observed superior performance.

3. Stability of Spherical Convolutional Filters

Adopting the spherical convolution as the main operation to process spherical signals exploits the rotational structure of 3D data and thus exhibits improved performance. In this section, we analyze the effect that structure perturbations in spherical signals have on the output of spherical convolutional filters, to explain theoretical reasons behind its superior performance.

3.1. Rotation equivariance

We begin by considering rotation operations as fundamental structure perturbations in spherical signals. Let $r \in \text{SO}(3)$ be a rotation and x be a spherical signal. Define the rotated signal x_r as

$$x_r(u) = x(r(u)) = x(\theta_u + r^\theta(\theta_u, \phi_u), \phi_u + r^\phi(\theta_u, \phi_u)), \forall u \in \mathbb{S}_2, \quad (12)$$

where the last equality responds to the rotation displacements following the Rodrigues' formula [cf. (2)]. We formally state the rotation equivariance of spherical convolutional filters in the following proposition.

Proposition 1. *Let x be a spherical signal, H be a spherical convolutional filter, and $r \in \text{SO}(3)$ be a rotation. Denote by $y = H(x)$ the filter output and y_r the rotated signal of y [cf. (12)]. Then, it holds that*

$$y_r = H(x_r). \quad (13)$$

Proof. See Appendix A for a detailed proof that completes that in [16, 17]. \square

Proposition 1 states that applying a spherical convolutional filter H to a rotated version of the signal $H(x_r)$ yields an associated rotated version of the output y_r , where $y = H(x)$ is the output of filtering the original signal. This indicates that the spherical convolutional filter is capable of harnessing the same information irrespective of what rotated version of the spherical signal is processed. The rotation equivariance serves to improve transference and speed up training, since learning how to process one instance of the signal is equivalent to learning how to process all rotated versions of the same signal. This is analogous

to the effect that translation equivariance has on CNNs [30] and the effect that permutation equivariance has on GNNs [38].

3.2. Signal dissimilarity modulo rotations

In general, we are more interested in how Spherical CNNs fare when acting on two signals that are similar but not quite the same. In a sense, we expect the architecture to tell apart spherical signals when they are sufficiently different but to give a similar output if the signal change is due to noise or unimportant causes [39, 40, 41]. The rotation equivariance (Prop. 1) states that the same information is obtained when processing all rotated versions of the same signal. This suggests that to measure how (dis)similar two signals are, we need to abstract rotations or, in other words, we need to do it modulo rotations. Motivated by this consideration, we define the rotation distance as follows.

Definition 1 (Rotation distance). *For two spherical signals x, \hat{x} , the rotation distance is defined as*

$$\|x - \hat{x}\|_{\text{SO}(3)} = \inf_{r \in \text{SO}(3)} \|x - \hat{x}_r\| \quad (14)$$

where $\hat{x}_r(u) = \hat{x}(r(u))$ is the rotated spherical signal of \hat{x} by the rotation r and $\|\cdot\|$ is the norm representation.

Any valid norm can be applied in the rotation distance (Def. 1). In the case of spherical signals, we adopt the normalized spherical norm.

Definition 2 (Normalized spherical norm). *For a spherical signal $x : \mathbb{S}_2 \rightarrow \mathbb{R}$, the normalized spherical norm is defined as*

$$\|x\|^2 = \frac{1}{2\pi^2} \int x(\theta_u, \phi_u)^2 d\theta_u d\phi_u. \quad (15)$$

where $\theta_u \in [0, \pi]$ and $\phi_u \in [0, 2\pi)$ describe the support of the spherical signal x in the spherical coordinate system [cf. (1)]. For multi-feature spherical signals $\mathbf{x} = \{x^f\}_{f=1}^F$, we define $\|\mathbf{x}\|^2 = \sum_{f=1}^F \|x^f\|^2$.

This is a proper norm in the sense that it is (i) absolutely scalable, (ii) positive definite, and (iii) satisfying the triangular inequality. Equipping spherical signals with a norm allows us to define the following normed space

$$\mathbb{L}^2(\mathbb{S}_2) = \{\mathbf{x} : \mathbb{S}_2 \rightarrow \mathbb{R}^F : \|\mathbf{x}\| < \infty\}. \quad (16)$$

The $\mathbb{L}^2(\mathbb{S}_2)$ space holds for single-feature signals by setting $F = 1$ in (16) and using the corresponding definition of the normalized spherical norm [cf. Def. 2]. In essence, $\mathbb{L}^2(\mathbb{S}_2)$ is the space of all finite-energy spherical signals.

Note that, if $\hat{x}(u) = x(r(u)) = x_r(u)$ is a rotated version of the spherical signal x by r , then $\|x - \hat{x}\|_{\text{SO}(3)} = \|x - x_r\|_{\text{SO}(3)} = 0$. Under this dissimilarity measure given by the rotation distance (Def. 1), Prop. 1 can be reframed with respect to the following corollary.

Corollary 1. *Let x, \hat{x} be two spherical signals, and H be a spherical convolutional filter. Then, it holds that*

$$\|x - \hat{x}\|_{\text{SO}(3)} = 0 \Rightarrow \|H(x) - H(\hat{x})\|_{\text{SO}(3)} = 0. \quad (17)$$

Proof. See Appendix B. □

Note that the rotation distance [cf. (14)] applies to the filter output since the latter is also a spherical signal.

Remark 2 (Group distance). Definition 1 can be extended to any group. In particular, let $\mathbf{G} = \mathbf{G}(\mathbb{X}, \circ)$ be a group with elements $g \in \mathbf{G}$ defined over space \mathbb{X} , and $x, \hat{x} : \mathbb{X} \rightarrow \mathbb{R}$ be two group signals mapping \mathbb{X} to the real line \mathbb{R} . The group distance with respect to \mathbf{G} is defined as

$$\|x - \hat{x}\|_{\mathbf{G}} = \inf_{g \in \mathbf{G}} \|x - \hat{x}_g\| \quad (18)$$

where $\hat{x}_g(u) = \hat{x}(g(u))$ is the signal operated by g and $\|\cdot\|$ can be any valid norm. The rotation distance is a particular case of this definition for $\mathbf{G} = \text{SO}(3)$.

3.3. Stability to diffeomorphism perturbations

With above preliminaries in place, we formally characterize the stability of Spherical CNNs to general structure perturbations under the rotation distance

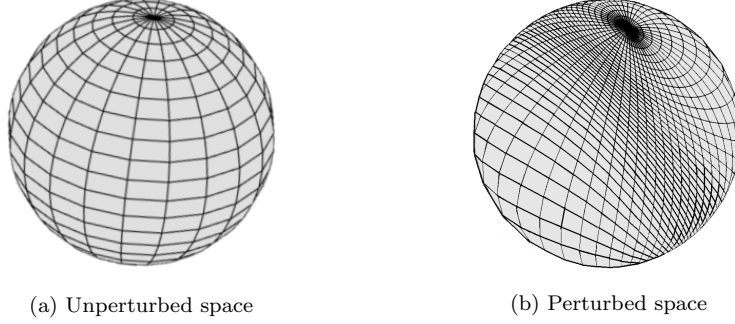


Figure 3. Diffeomorphism perturbation on the sphere [cf. Def 3]. (a) Unperturbed sphere. (b) Perturbed sphere after a diffeomorphism perturbation.

(Def. 1). In other words, we shift focus on arbitrary structure perturbations that are different from but close to rotation operations.

We consider the general structure perturbation $\tau : \mathbb{S}_2 \rightarrow \mathbb{S}_2$ that displaces each point $u \in \mathbb{S}_2$ to another point $\tau(u) \in \mathbb{S}_2$. Such a perturbation can be represented as a set of local rotations, i.e., the rotation whose characterization changes depending on the specific point $u \in \mathbb{S}_2$ on which it is applied to. Let $r_u \in \text{SO}(3)$ be the rotation operation that maps the point $u_0 = (0, 0) \in \mathbb{S}_2$ to the point $u \in \mathbb{S}_2$ along the shortest arc, i.e., $r_u(u_0) = u$, and similarly $r_{\tau(u)}$ be the rotation operation that maps the point u_0 to the perturbed point $\tau(u)$ along the shortest arc, i.e., $r_{\tau(u)}(u_0) = \tau(u)$. Combining the notions of r_u and $r_{\tau(u)}$, we can formally define the general structure perturbation as the diffeomorphism perturbation in the following definition.

Definition 3 (Diffeomorphism perturbation). *Let $\tau : \mathbb{S}_2 \rightarrow \mathbb{S}_2$ be a diffeomorphism, i.e., a bijective differentiable function whose inverse $\tau^{-1} : \mathbb{S}_2 \rightarrow \mathbb{S}_2$ is differentiable as well. The diffeomorphism is equivalent to a set of local rotations $\{\tau_u\}_{u \in \mathbb{S}_2}$, where each local rotation $\tau_u \in \text{SO}(3)$ is defined as*

$$\tau_u = r_{\tau(u)} \circ r_u^{-1}, \quad \forall u \in \mathbb{S}_2, \quad (19)$$

that maps the point u to the perturbed point $\tau(u)$, i.e., $\tau(u) = \tau_u(u)$ for all $u \in \mathbb{S}_2$. The diffeomorphism perturbation is defined as the set of local rotations

in (19) that satisfies $\|\tau\| < \infty$ and $\|\nabla\tau\| < \infty$ for

$$\|\tau\| := \max_{u \in \mathbb{S}_2} \left\{ \beta^{\tau_u} \right\}, \quad (20)$$

where β^{τ_u} is the rotation angle of the local rotation τ_u [cf. (19)]²; and for

$$\|\nabla\tau\| = \max_{(\theta_u, \phi_u) \in [0, \pi] \times [0, 2\pi)} \left\{ \left| \frac{\partial \tau^\theta}{\partial \theta_u} \right|, \left| \frac{\partial \tau^\phi}{\partial \phi_u} \right| \right\}. \quad (21)$$

where τ^θ and τ^ϕ are polar and azimuthal angle displacements induced by τ such that $\tau^\theta(\theta_u, \phi_u) = \tau_u^\theta(\theta_u, \phi_u)$ and $\tau^\phi(\theta_u, \phi_u) = \tau_u^\phi(\theta_u, \phi_u)$ for all $u \in \mathbb{S}_2$. The signal resulting from a diffeomorphism perturbation to the spherical structure of a given signal x is denoted by x_τ such that

$$x_\tau(u) = x(\tau(u)) = x(\tau_u(u)), \quad \forall u \in \mathbb{S}_2. \quad (22)$$

The diffeomorphism perturbation (Def. 3) is, essentially, a set of local rotations where rotation axes and rotation angles depend on specific points on the sphere. We remark that since rotations can displace a point $u \in \mathbb{S}_2$ to any other point on the sphere, this representation can model any structure perturbation in the spherical space. Under the rotation distance [cf. (14)], we have

$$\|x - x_\tau\|_{\text{SO}(3)} = \inf_{r \in \text{SO}(3)} \|x - x_{\tau \circ r}\|. \quad (23)$$

Thus, if we want to measure the *size of the perturbation*, we need to do so modulo rotations. Define the closest rotation r^* to the diffeomorphism τ as

$$r^* = \underset{r \in \text{SO}(3)}{\operatorname{argmin}} \max\{\|\tau \circ r^{-1}\|, \|\nabla(\tau \circ r^{-1})\|\} \quad (24)$$

where $\tau \circ r^{-1}$ is also a diffeomorphism but modulo the rotation r . The *perturbation size* modulo rotations is then measured by [cf. (20), (21)]

$$\|\tau\|_{\text{SO}(3)} = \|\tau \circ (r^*)^{-1}\|, \quad \|\nabla\tau\|_{\text{SO}(3)} = \|\nabla(\tau \circ (r^*)^{-1})\|. \quad (25)$$

In this way, (25) links the perturbation size to the rotation distance [cf. (14)] and determines how far from a rotation the actual perturbation τ is. Note that

²The rotation angle β^{τ_u} indicates the maximal geodesic distance that can be induced by the local rotation τ_u on the unit sphere.

if the diffeomorphism perturbation is the rotation operation, all local rotations are same and $\|\tau\|_{\text{SO}(3)} = \|\nabla\tau\|_{\text{SO}(3)} = 0$. Likewise, $\|\tau\|_{\text{SO}(3)} = \|\nabla\tau\|_{\text{SO}(3)} = 0$ implies that the diffeomorphism perturbation is the rotation, i.e., $\tau \in \text{SO}(3)$. An example of the diffeomorphism perturbation is illustrated in Fig. 3.

We have now defined the diffeomorphism perturbations of the spherical signal, as those that modify the spherical space \mathbb{S}_2 by using local rotations, i.e. rotations whose axes and angles vary as specific points in the spherical space change [cf. Def. 3]. Next, we restrict our attention to the family of *Lipschitz* filters.

Definition 4 (Lipschitz filter). *A spherical convolutional filter $h : \mathbb{S}_2 \rightarrow \mathbb{R}$ is Lipschitz, if there exists a constant C_h such that*

$$|h(u)| \leq C_h, \quad \frac{|h(u_1) - h(u_2)|}{\text{arc}(u_1, u_2)} \leq C_h \quad (26)$$

for all $u, u_1, u_2 \in \mathbb{S}_2$, where $\text{arc}(u_1, u_2)$ is the length of the shortest arc between u_1 and u_2 on the sphere. When we consider multi-feature signals, we say a filter H [cf. (11)] is Lipschitz if each of the FG single-feature filters h^{fg} satisfies (26).

We can now proceed to characterize the stability of spherical convolutional filters to diffeomorphism perturbations [cf. Def. 3] in the input spherical signal.

Theorem 1 (Stability of spherical filters). *Let $x \in \mathbb{L}^2(\mathbb{S}_2)$ be a spherical signal, and H be a Lipschitz filter with constant C_h [cf. Def 4]. Consider the diffeomorphism perturbation τ [cf. Def 3] that satisfies*

$$\|\tau\|_{\text{SO}(3)} \leq \epsilon, \quad \|\nabla\tau\|_{\text{SO}(3)} \leq \epsilon \leq \frac{1}{2}. \quad (27)$$

Then, for the perturbed input spherical signal x_τ [cf. (22)], it holds that

$$\|H(x) - H(x_\tau)\|_{\text{SO}(3)} \leq 8C_h\epsilon\|x\| + \mathcal{O}(\epsilon^2) \quad (28)$$

Proof. See Appendix C. □

Theorem 1 establishes that spherical convolution filters are Lipschitz stable to diffeomorphism perturbations (modulo rotations). More specifically, the output difference between filtering x and a perturbed version x_τ of it, is bounded

linearly by the perturbation size ϵ with respect to the stability constant $8C_h$. When the diffeomorphism perturbation is close to the rotation operation (i.e., $\epsilon \rightarrow 0$), the bound approaches zero and the spherical convolutional filter maintains performance. The stability constant implies the role of the filter property. A careful design can reduce the Lipschitz constant C_h and thus, lead to more stable filters. The constant term 8 depends on the domain, which can be improved by further restricting the class of filters. Note that Theorem 1 reduces to Corollary 1 if the diffeomorphism perturbation τ reduces to the rotation operation r , i.e. $\|\tau\|_{\text{SO}(3)} = \|\nabla\tau\|_{\text{SO}(3)} = 0$.

In summary, Theorem 1 demonstrates that spherical convolutional filters yield similar (stable) outputs when signals are close to being rotated versions of each other. The result provides the stability analysis for arbitrary structure perturbations in spherical signals, where the rotation equivariance is a special case when particularizing structure perturbations as rotation operations. In other words, we extend the rotation equivariance to general stability property.

4. Stability of Spherical Convolutional Neural Networks

Spherical CNNs $\Phi(x; \mathcal{H})$ [cf. (10)] are nonlinear processing architectures consisting of spherical convolutional filters and pointwise nonlinearities, which have the potential to learn nonlinear representations from spherical signals. Based on the stability result of spherical convolutional filters, we characterize the effect of structure perturbations on the output of Spherical CNNs, to illustrate how they exploit the rotational structure inherent in spherical signals.

4.1. Rotation equivariance of Spherical CNNs

The fact that spherical convolutional filters are rotation equivariant (Prop. 1) extends immediately to Spherical CNNs. This is because of the pointwise nature of the nonlinearity, which does not affect the data structure.

Proposition 2. *Let x be a spherical signal, $\Phi(\cdot; \mathcal{H})$ be a Spherical CNN [cf. (10)], and $r \in \text{SO}(3)$ be a rotation. Denote by $x_r(u) = x(r(u)) \forall u \in \mathbb{S}_2$ the*

rotated version of the input spherical signal x by r . Then, it holds that

$$\|\Phi(x; \mathcal{H}) - \Phi(x_r; \mathcal{H})\|_{\text{SO}(3)} = 0. \quad (29)$$

Proof. See Appendix D. \square

Proposition 2 demonstrates that the output of Spherical CNN applied on the rotated spherical signal $y = \Phi(x_r; \mathcal{H})$ is the corresponding rotated output of Spherical CNN applied on the unperturbed spherical signal $y_r(u) = y(r(u))$ for all $u \in \mathbb{S}_2$. This implies that Spherical CNNs capture the same information, irrespective of the specific rotated version of spherical signal. Proposition 2 suggests that Spherical CNNs generalize well since they can learn how to process all rotated versions of a given signal, by learning how to process one of them.

4.2. Stability to diffeomorphism perturbations of Spherical CNNs

We proceed to consider general structure perturbations instead of fundamental rotation operations. The stability of Spherical CNNs to diffeomorphism perturbations (Def. 3) is inherited from that of spherical convolutional filters. The inclusion of nonlinearity in the architecture affects the stability constant. In particular, we consider the Lipschitz nonlinearity as defined next.

Definition 5 (Lipschitz nonlinearity). *A nonlinearity $\sigma : \mathbb{R} \rightarrow \mathbb{R}$ satisfying $\sigma(0) = 0$ is Lipschitz if there exists a constant $C_\sigma > 0$ such that*

$$|\sigma(a) - \sigma(b)| \leq C_\sigma |a - b|, \quad \forall a, b \in \mathbb{R}. \quad (30)$$

When Spherical CNNs are built from Lipschitz filters (Def. 4) and use Lipschitz nonlinearities (Def. 5), they inherit the stability to diffeomorphism perturbations (Def. 3) from spherical convolutional filters [cf. Theorem 1].

Theorem 2 (Stability of Spherical CNNs). *Let $x \in \mathbb{L}^2(\mathbb{S}_2)$ be a spherical signal, and $\Phi(\cdot; \mathcal{H})$ be a Spherical CNN [cf. (10)] consisting of L layers, with $F_\ell = F$ features per layer, built with Lipschitz filters with constant C_h [cf. Def 4] and*

Lipschitz nonlinearities with constant C_σ [cf. Def. 5]. Consider a diffeomorphism perturbation τ [cf. Def 3] that satisfies

$$\|\tau\|_{\text{SO}(3)} \leq \epsilon, \quad \|\nabla\tau\|_{\text{SO}(3)} \leq \epsilon \leq \frac{1}{2}. \quad (31)$$

Then, for the perturbed input spherical signal x_τ [cf. (22)], it holds that

$$\|\Phi(x; \mathcal{H}) - \Phi(x_\tau; \mathcal{H})\|_{\text{SO}(3)} \leq 8C_h^L C_\sigma^L F^{L-1} \epsilon \|x\| + \mathcal{O}(\epsilon^2). \quad (32)$$

Proof. See Appendix E. □

Theorem 2 determines that Spherical CNNs are Lipschitz stable to structure perturbations. More specifically, the output difference of Spherical CNN induced by diffeomorphism perturbations (modulo rotations) is upper bounded by a term that depends proportionally on the size of the perturbation ϵ . When the perturbation size $\epsilon \rightarrow 0$, diffeomorphism perturbations approach rotation operations, the bound reduces to zero, and Spherical CNNs maintain performance. In other words, if two signals are close to being rotated versions of each other, their outputs of the Spherical CNN will be close as well.

While the stability bound may have a similar form as that of spherical convolutional filters [Thm. 1], the stability constant accounts for the effects of different architecture components. In particular, it is the product of three terms:

- (1) The first term $8C_h^L$ captures the property of spherical convolutional filters. A larger Lipschitz constant C_h [cf. (26)] allows larger input-output expansivity through filtering propagation and more variability in filter values between nearby spherical points, leading to less stability to structure perturbations that displace spherical points arbitrarily. Reducing C_h yields spherical convolutional filters that are less expansive and change more slowly, resulting in the improved stability. However, this improvement comes at expenses of the information loss and the expressive power. The former is because less expansive filters propagate less information from the input to the output, and the latter is because filters become more flat in the spherical surface reducing the representative power.

- (2) The term C_σ^L captures the role of the nonlinearity. In particular, C_σ is typically one indicating the non-expansivity of the nonlinearity, such as the absolute value, the ReLU, the Tanh, etc.
- (3) The last term F^{L-1} represents the impact of the Spherical CNN architecture, namely, the number of layers (L) and the number of spherical convolutional filters per layer (F). A wider architecture with more features and a deeper architecture with more layers yields a looser bound and degrades the stability. This can be explained by the fact that more filters are involved in the Spherical CNN, which amplifies the effect of structure perturbations passing through the architecture.

Overall, Spherical CNNs inherit the stability to structure perturbations from spherical convolutional filters. This explains how Spherical CNNs exploit the underlying structure present in 3D data and how they maintain performance under arbitrary perturbations close to rotations.

Remark 3. The results can be extended to any generic group G besides the rotation group $SO(3)$. I.e., the stability to general diffeomorphism perturbations applies to the group convolutional filter [cf. (8)]; hence, applies to the group convolutional neural network. Proofs of propositions and theorems can be carried out with similar processes, while the key step may be to find a suitable mathematical representation for the data structure of interest to perform theoretical analysis. In the rotation group $SO(3)$, for instance, the spherical coordinate system is utilized to describe spherical signals and the Euler parameterization is used to characterize the rotation operation.

5. Numerical Experiments

We have proved that Spherical CNNs are stable to general structure perturbations (i.e., diffeomorphism perturbations). This illustrates how Spherical CNNs exploit the data structure to improve representative power and learning

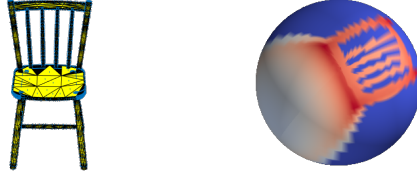


Figure 4. 3D model (left) and spherical signal (right) of a chair.

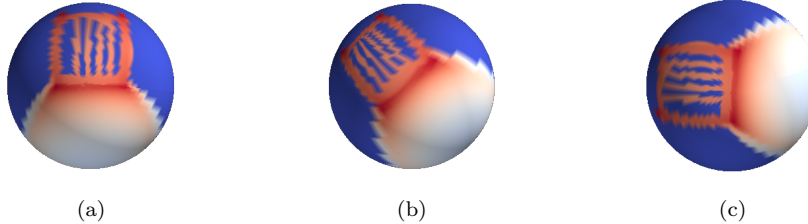


Figure 5. Rotation operations on the spherical signal. (a) 45 degree rotation. (b) 90 degree rotation. (c) 135 degree rotation.

capacity. As a matter of fact, they have already been shown successful in classification tasks [16]. Thus, in what follows, we focus solely on corroborating the stability property by numerical experiments with admissible perturbations; for performance comparison with other learning methods, please refer to [16].

Problem setting and dataset. The shape classification problem of 3D object is considered on ModelNet40 dataset [25], i.e., given a spherical signal, the goal is to find out which class its represented object belongs to. There are 40 classes in the dataset, where we use 9683 samples for training and 29595 samples for testing. We parametrize the spherical signal in a 64×64 resolution—see Fig. 4 for the 3D model of a chair and the associated spherical signal.

Architectures and training. We consider the Spherical CNN of 8 layers, each containing 16, 16, 32, 32, 64, 64, 128 and 128 spherical convolutional filters and the ReLU nonlinearity. At the readout layer, we apply a global weighted average pooling for a descriptor vector and the latter is projected into the number of object classes. We train the architecture for 50 epochs with the ADAM optimizer and a batch size of 16 samples. The learning rate is

Table 1: Test classification accuracy of the Spherical CNN for the original data, 45 degree rotated data, 90 degree rotated data, and 135 degree rotated data. Root mean square error (RMSE) of the Spherical CNN output features for the 45 degree rotated data, 90 degree rotated data and 135 degree rotated data.

Rotation angle	Classification accuracy	RMSE
0 degree	0.864	0
45 degree	0.864	$1.67 \cdot 10^{-3}$
90 degree	0.864	$1.58 \cdot 10^{-3}$
135 degree	0.864	$2.67 \cdot 10^{-3}$

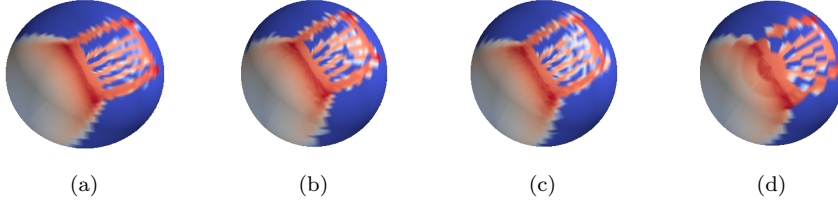


Figure 6. Diffeomorphism perturbations on the spherical signal. (a) Type 1. (b) Type 2. (c) Type 3. (d) Type 4.

$1 \cdot 10^{-3}$, which is divided by 5 on epochs 30 and 40 respectively. We start by considering structure perturbations as fundamental rotation operations, and proceed to arbitrary diffeomorphism perturbations.

Rotation equivariance. Given a trained Spherical CNN, we consider the testing data perturbed by 45 degree, 90 degree and 135 degree rotation operations, respectively. Fig. 5 displays the resulting spherical signals under three rotations, and Table 1 shows the classification accuracies over the original and rotated testing data. We see that the classification accuracies remain the same, evidencing that the Spherical CNN is rotation equivariant. We also show the root mean squared error (RMSE) between output features of the Spherical CNN when applied to the original signal and the rotated signal. The results indicate that they are virtually the same output features, as expected in theory.

Table 2: Test classification accuracy of the Spherical CNN for diffeomorphism perturbation types 1-4. Root mean square error (RMSE) of the Spherical CNN output features for diffeomorphism perturbation types 1-4.

Diffeomorphism perturbation	Classification accuracy	RMSE
Type 1	0.863	0.0668
Type 2	0.856	0.0872
Type 3	0.858	0.0778
Type 4	0.828	0.1254

Diffeomorphism perturbations. We now test the output change of the Spherical CNN when the input signal is subject to four types of diffeomorphism perturbations. Namely, we carry out different local rotations along the latitude, indicating different perturbation severity. For type 1, we rotate every other sampled point at each latitude with a random degree drawn from $[-3, 3]$, where we assume the clockwise direction as the positive direction. Type 2 rotates every other sampled point with a random degree drawn from $[-6, 6]$. Type 3 considers the local rotation at each sampled point with a random degree drawn from $[-3, 3]$. Finally, type 4 perturbs blocks of 3 samples at each latitude separately, rotating the second point to the third point and interpolating the values of the remaining sampled point, where the maximal degree change is approximately 6 degrees. Fig. 6 displays perturbed spherical signals that are associated to these four types of diffeomorphism perturbations.

Diffeomorphism stability. Table 2 shows the classification accuracies of the trained Spherical CNN when assuming that testing spherical signals are perturbed by aforementioned four types of diffeomorphism perturbations. In general, the Spherical CNN exhibits strong robustness in four cases, as expected from Theorem 2. We see that type 1 has little effect on the classification accuracy, while types 2 and 3 slightly decrease the accuracy due to the increase of the maximal degree change and the increased number of perturbed sampled points. Type 4 is most severe as observed from Fig. 6d, while the Spherical

CNN only suffers from 0.036 accuracy loss, emphasizing its stability to diffeomorphism perturbations. Table 2 also shows the RMSE of the output features at final layer under above diffeomorphism perturbations. The RMSE maintains low values in all cases, which validates the stability of the Spherical CNN to diffeomorphism perturbations.

6. Conclusions

This paper investigated the stability of Spherical CNNs to general structure perturbations in spherical signals. We first considered spherical signals perturbed by fundamental rotation operations, and proved explicitly the output of the Spherical CNN applied on the rotated signal is the rotated output of the Spherical CNN applied on the unperturbed signal. This property, referred to as the rotation equivariance, implies the same information is obtained irrespective of rotation operations and thus, we defined the rotation distance for stability analysis modulo rotations. We then considered spherical signals perturbed by arbitrary structure perturbations, and modelled the latter as diffeomorphism perturbations. We showed the output difference of Spherical CNN induced by the diffeomorphism perturbation is upper bounded proportionally by the perturbation size under the rotation distance. This result indicates that Spherical CNNs maintain performance when structure perturbations are close to rotation operations. These theoretical findings also show the explicit role of the filter property, nonlinearity, architecture width and depth on the stability of Spherical CNNs, which identifies handle to improve the robustness. The theory was corroborated through numerical experiments of 3D object classification.

Appendix A. Proof of Proposition 1

Proof. Given the rotated spherical signal x_r , the output of the spherical convolutional filter H is given by

$$\begin{aligned} H(x_r)(u) &= \int_{\text{SO}(3)} h(\hat{r}^{-1}(u)) x(r(\hat{r}(u_0))) d\hat{r} \\ &= \int_{\text{SO}(3)} h((r \circ \hat{r})^{-1}(r(u))) x((r \circ \hat{r})(u_0)) d\hat{r}, \end{aligned} \quad (\text{A.1})$$

where $u_0 = (0, 0) \in \mathbb{S}_2$ is given by $\theta_{u_0} = \phi_{u_0} = 0$ and $r(u) \in \mathbb{S}_2$ is the rotated point of u by r . By defining $r' = r \circ \hat{r}$, we can rewrite (A.1) as

$$\begin{aligned} H(x_r)(u) &= \int_{\text{SO}(3)} h(r'^{-1}(r(u))) x(r'(u_0)) dr' \\ &= h *_{\text{SO}(3)} x(r(u)) = H(x)(r(u)) \end{aligned} \quad (\text{A.2})$$

Note that (A.2) holds for any point $u \in \text{SO}(3)$, and thus it holds for the spherical signal x . By letting $y = H(x)$, we complete the proof that $H(x_r) = y_r$. \square

Appendix B. Proof of Corollary 1

Proof. Given $\|x - \hat{x}\|_{\text{SO}(3)} = 0$ under the rotation distance [Def. 2], there exists a rotation \hat{r} such that $\hat{x} = x_{\hat{r}}$ is a rotated version of signal x . Denote by $y = H(x)$ the output of spherical convolutional filter and we have $H(x_{\hat{r}}) = y_{\hat{r}}$ resulting from Proposition 1. Under the rotation distance, we get

$$\|H(x) - H(\hat{x})\|_{\text{SO}(3)} = \inf_{r \in \text{SO}(3)} \|y - y_{\hat{r} \circ r}\| \leq \|y - y_{\hat{r} \circ \hat{r}^{-1}}\| = 0. \quad (\text{B.1})$$

Since $\|H(x) - H(\hat{x})\|_{\text{SO}(3)} \geq 0$ by the norm definition, we can then obtain $\|H(x) - H(\hat{x})\|_{\text{SO}(3)} = 0$ completing the proof. \square

Appendix C. Proof of Theorem 1

Proof. Under the rotation distance, the output difference of the spherical convolutional filter induced by the diffeomorphism perturbation τ is

$$\begin{aligned} \|H(x_\tau) - H(x)\|_{\text{SO}(3)} &= \inf_{r \in \text{SO}(3)} \|H(x_\tau) - (H(x))_r\| \\ &= \inf_{r \in \text{SO}(3)} \|H(x_\tau) - H(x_r)\| \leq \|H(x_\tau) - H(x_{r^*})\| \end{aligned} \quad (\text{C.1})$$

where $(H(x))_r$ is the rotated version of the filter output $H(x)$ by r , and where the rotation equivariance of the spherical convolutional filter is used and $r^* \in \text{SO}(3)$ is the closest rotation to τ defined as $r^* = \operatorname{argmin}_{r \in \text{SO}(3)} \max\{\|\tau \circ r^{-1}\|, \|\nabla(\tau \circ r^{-1})\|\}$ [cf. (24)]. Since the normalized spherical norm is rotation invariant, i.e., $\|x_r\| = \|x\|$ for all $r \in \text{SO}(3)$, we have

$$\begin{aligned} \|H(x_\tau) - H(x_{r^*})\| &= \|(H(x_\tau))_{(r^*)^{-1}} - (H(x_{r^*}))_{(r^*)^{-1}}\| \\ &= \|H(x_{\tau \circ (r^*)^{-1}}) - H(x_{r^* \circ (r^*)^{-1}})\| = \|H(x_{\tau \circ (r^*)^{-1}}) - H(x)\| \end{aligned} \quad (\text{C.2})$$

where $(H(x))_{(r^*)^{-1}}$ is the rotated version of the filter output $H(x)$ by $(r^*)^{-1}$. Let $\tau^* = \tau \circ (r^*)^{-1}$ be the diffeomorphism module the rotation r^* . Let also $Hx = H(x)$ and $P_\tau^* x = x_{\tau^*}$ be operator notations. By substituting (C.2) into (C.1), we get

$$\|H(x_\tau) - H(x)\|_{\text{SO}(3)} \leq \|HP_\tau^* x - Hx\| = \|(HP_\tau^* - H)x\|. \quad (\text{C.3})$$

We consider the operator $HP_\tau^* - H$ and factorize it as

$$HP_\tau^* - H = (H - HP_\tau^{*-1})P_\tau^*. \quad (\text{C.4})$$

where P_τ^{*-1} is the inverse operator of P_τ^* , which exists since τ^* is a diffeomorphism. The triangle inequality allows

$$\|HP_\tau^* - H\| = \|(H - HP_\tau^{*-1})P_\tau^*\| \leq \|P_\tau^*\| \|H - HP_\tau^{*-1}\|. \quad (\text{C.5})$$

Let us analyze two terms in the bound of (C.5) separately.

For the first term $\|P_\tau^*\|$, a known procedure to bound the norm of an operator P_τ^* is to find an upper bound of $\|P_\tau^* x\|$ as $\|P_\tau^* x\| \leq A\|x\|$ for any spherical signal x . Then, A is the upper bound of $\|P_\tau^*\|$. Following this intuition, we have

$$\begin{aligned} \|P_\tau^* x\|^2 &= \frac{1}{2\pi^2} \int P_\tau^* x(\theta_u, \phi_u)^2 d\theta_u d\phi_u \\ &= \frac{1}{2\pi^2} \int x(\theta_u + \tau^{*\theta}(\phi_u, \theta_u), \phi_u + \tau^{*\phi}(\phi_u, \theta_u))^2 d\theta_u d\phi_u \end{aligned} \quad (\text{C.6})$$

where $\tau^{*\theta}$ and $\tau^{*\phi}$ are polar and azimuth angle displacements induced by τ^* . Denote by $\hat{\theta}_u = \theta_u + \tau^{*\theta}(\phi_u, \theta_u)$ and $\hat{\phi}_u = \phi_u + \tau^{*\phi}(\phi_u, \theta_u)$ the variable substi-

tutions, and observe that

$$\begin{aligned} d\hat{\theta}_u d\hat{\phi}_u &= \left(1 + \frac{\partial \tau^{*\theta}}{\partial \theta_u}(\theta_u, \phi_u)\right) \left(1 + \frac{\partial \tau^{*\phi}}{\partial \phi_u}(\theta_u, \phi_u)\right) d\theta_u d\phi_u \\ &\geq (1 - \|\nabla \tau\|_{\text{SO}(3)})^2 d\theta_u d\phi_u, \end{aligned} \quad (\text{C.7})$$

where the last inequality is due to the definition of $\|\nabla \tau\|_{\text{SO}(3)}$ [cf. (25)]. Substituting (C.7) into (C.6) yields

$$\begin{aligned} \|P_\tau^* x\|^2 &\leq \frac{1}{2\pi^2} \int x(\hat{\theta}_u, \hat{\phi}_u)^2 (1 - \|\nabla \tau\|_{\text{SO}(3)})^{-2} d\hat{\theta}_u d\hat{\phi}_u \\ &= (1 - \|\nabla \tau\|_{\text{SO}(3)})^{-2} \|x\|^2 \leq 4\|x\|^2, \end{aligned} \quad (\text{C.8})$$

where $\|\nabla \tau\|_{\text{SO}(3)} \leq 1/2$ is used in the last inequality. Thus, we have $\|P_\tau^*\| \leq 2$.

For the second term $\|H - HP_\tau^{*-1}\|$, let $P_\tau^{*-1}x(u) = x(\xi(u))$ where ξ is the inverse operation of τ^* , and we have

$$Hx(u) = \int_{\text{SO}(3)} h(r^{-1}(u))x(r(u_0))dr, \quad (\text{C.9})$$

$$HP_\tau^{*-1}x(u) = \int_{\text{SO}(3)} h(r^{-1}(u))x(\xi(r(u_0)))dr. \quad (\text{C.10})$$

where $u_0 = (0, 0)$ is the point given by $\theta_u = \phi_u = 0$. For (C.9), we can rewrite it by parametrizing rotations with the Euler angles [cf. (3) and (7)] as

$$\begin{aligned} Hx(u) &= \frac{1}{8\pi^2} \int h\left(r_{\phi_r \theta_r \rho_r}^{-1}(u)\right) x(\theta_r, \phi_r) \sin(\theta_r) d\theta_r d\phi_r d\rho_r \\ &= \frac{1}{8\pi^2} \int h\left((r_{u_r} \circ r_{\rho_r}^z)^{-1}(u)\right) x(\theta_r, \phi_r) \sin(\theta_r) d\theta_r d\phi_r d\rho_r \end{aligned} \quad (\text{C.11})$$

where $r_{\phi_r \theta_r \rho_r}$ is the rotation characterized by the Euler angles $(\phi_r, \theta_r, \rho_r)$ and $r_{\phi_r \theta_r \rho_r}^{-1}$ is its inverse rotation, and where r_{u_r} is the rotation that rotates the point $u_0 = (0, 0)$ to the point $u_r = (\theta_r, \phi_r)$ along the shortest arc, i.e., $r_{u_r}(u_0) = u_r$, $r_{\rho_r}^z$ is the rotation along z -axis by ρ_r angles, and $(r_{u_r} \circ r_{\rho_r}^z)^{-1} = r_{\rho_r}^{z^{-1}} \circ r_{u_r}^{-1}$ is its inverse rotation. For (C.10), by letting $\xi_r = \xi \circ r$, we have

$$HP_\tau^{*-1}x(u) = \int_{\text{SO}(3)} h(r^{-1}(u))x(\xi_r(u_0))dr. \quad (\text{C.12})$$

Let $\xi_r(u_0) = u_r = (\theta_r, \phi_r)$ be the polar angle displacement and the azimuth angle displacement of ξ_r at u_0 . Since $\xi^{-1} = \tau^*$, we get

$$r(u_0) = \xi^{-1}(\xi_r(u_0)) = \tau^*(u_r) = (\theta_r + \tau^{*\theta}(\theta_r, \phi_r), \phi_r + \tau^{*\phi}(\theta_r, \phi_r)) \quad (\text{C.13})$$

such that the normalized Haar measure is given by

$$dr = \frac{1}{8\pi^2} \alpha(\theta_r, \phi_r) \sin(\theta_r + \tau^{*\theta}(\theta_r, \phi_r)) d\phi_r d\theta_r d\rho_r, \quad (\text{C.14})$$

with $\alpha(\theta_r, \phi_r) = \left(1 + \frac{\partial \tau^{*\theta}(\theta_r, \phi_r)}{\partial \theta_r}\right) \left(1 + \frac{\partial \tau^{*\phi}(\theta_r, \phi_r)}{\partial \phi_r}\right)$. By parametrizing rotations with the Euler angles [cf. (3) and (7)] and using the results in (C.13) and (C.14), we can similarly rewrite (C.12) as

$$HP_\tau^{*-1}x(u) = \frac{1}{8\pi^2} \int x(\theta_r, \phi_r) \alpha(\theta_r, \phi_r) \sin(\theta_r + \tau^{*\theta}(\theta_r, \phi_r)) \cdot h\left((r_{\tau^*(u_r)} \circ r_{\rho_r}^z)^{-1}(u)\right) d\theta_r d\phi_r d\rho_r \quad (\text{C.15})$$

where $r_{\tau^*(u_r)}$ is the rotation that rotates the point $u_0 = (0, 0)$ to the point $\tau^*(u_r) = (\theta_r + \tau^{*\theta}(\theta_r, \phi_r), \phi_r + \tau^{*\phi}(\theta_r, \phi_r))$ along the shortest arc, i.e., $r_{\tau^*(u_r)}(u_0) = \tau^*(u_r)$, $r_{\rho_r}^z$ is the rotation along z -axis by ρ_r angles, and $(r_{\tau^*(u_r)} \circ r_{\rho_r}^z)^{-1} = r_{\rho_r}^{z^{-1}} \circ r_{\tau^*(u_r)}^{-1}$ is its inverse rotation.

By substituting (C.11) and (C.15) into the operator $Hx - HP_\tau^{*-1}x$, we get

$$\begin{aligned} Hx(u) - HP_\tau^{*-1}x(u) &= \frac{1}{8\pi^2} \int x(\theta_r, \phi_r) \left[h\left(r_{\rho_r}^{z^{-1}}(r_{u_r}^{-1}(u))\right) \sin(\theta_r) \right. \\ &\quad \left. - h\left(r_{\rho_r}^{z^{-1}}(r_{\tau^*(u_r)}^{-1}(u))\right) \alpha(\theta_r, \phi_r) \sin(\theta_r + \tau^{*\theta}(\theta_r, \phi_r)) \right] d\theta_r d\phi_r d\rho_r \\ &= \frac{1}{8\pi^2} \int k(\theta_r, \phi_r, \rho_r, \theta_u, \phi_u) x(\theta_r, \phi_r) d\theta_r d\phi_r d\rho_r \end{aligned} \quad (\text{C.16})$$

where $u = (\theta_u, \phi_u)$ in the spherical coordinate system and $k(\theta_r, \phi_r, \rho_r, \theta_u, \phi_u)$ is the kernel of the operator $H - HP_\tau^{*-1}$. Recall the Schur's Lemma [42]. For the operator K with kernel $k(\theta_r, \phi_r, \rho_r, \theta_u, \phi_u)$, if

$$\frac{1}{8\pi^2} \int |k(\theta_r, \phi_r, \rho_r, \theta_u, \phi_u)| d\theta_r d\phi_r d\rho_r \leq A, \quad (\text{C.17})$$

$$\frac{1}{2\pi^2} \int |k(\theta_r, \phi_r, \rho_r, \theta_u, \phi_u)| d\theta_u d\phi_u \leq A, \quad (\text{C.18})$$

we have $\|K\| \leq A$. We proceed by using the Schur's Lemma.

We divide $k(\theta_r, \phi_r, \rho_r, \theta_u, \phi_u)$ into two sub-operators as

$$\begin{aligned} k(\theta_r, \phi_r, \rho_r, \theta_u, \phi_u) &= k_1(\theta_r, \phi_r, \rho_r, \theta_u, \phi_u) + k_2(\theta_r, \phi_r, \rho_r, \theta_u, \phi_u) \\ &= (1 - \alpha(\theta_r, \phi_r)) h\left(r_{\rho_r}^{z^{-1}}(r_{u_r}^{-1}(u))\right) \sin(\theta_r) \\ &\quad + \alpha(\theta_r, \phi_r) \left[h\left(r_{\rho_r}^{z^{-1}}(r_{u_r}^{-1}(u))\right) \sin(\theta_r) - h\left(r_{\rho_r}^{z^{-1}}(r_{\tau^*(u_r)}^{-1}(u))\right) \sin(\theta_r + \tau^{*\theta}(\theta_r, \phi_r)) \right], \end{aligned} \quad (\text{C.19})$$

and analyze these two sub-operators separately.

For the first sub-operator $k_1(\theta_r, \phi_r, \rho_r, \theta_u, \phi_u)$, since $|\partial\tau^{*\theta}(\theta_r, \phi_r)/\partial\theta_r| \leq \|\nabla\tau\|_{\text{SO}(3)}$ and $|\partial\tau^{*\phi}(\theta_r, \phi_r)/\partial\phi_r| \leq \|\nabla\tau\|_{\text{SO}(3)}$ [cf. (25)], we have

$$|1 - \alpha(\theta_r, \phi_r)| \leq (2 + \|\nabla\tau\|_{\text{SO}(3)}) \|\nabla\tau\|_{\text{SO}(3)}. \quad (\text{C.20})$$

By substituting (C.20) into $k_1(\theta_r, \phi_r, \rho_r, \theta_u, \phi_u)$, we obtain

$$\begin{aligned} |k_1(\theta_r, \phi_r, \rho_r, \theta_u, \phi_u)| &\leq |1 - \alpha(\theta_r, \phi_r)| \left| h\left(r_{\rho_r}^{z^{-1}}(r_{u_r}^{-1}(u))\right) \right| \\ &\leq C_h (2 + \|\nabla\tau\|_{\text{SO}(3)}) \|\nabla\tau\|_{\text{SO}(3)} \leq 2C_h\epsilon + \mathcal{O}(\epsilon^2) \end{aligned} \quad (\text{C.21})$$

where the last inequality uses the conditions that h is a Lipschitz filter with respect to C_h and $\|\nabla\tau\|_{\text{SO}(3)} \leq \epsilon$.

For the second sub-operator $k_2(\theta_r, \phi_r, \rho_r, \theta_u, \phi_u)$, we have

$$|\alpha(\theta_r, \phi_r)| \leq 1 + 2\|\nabla\tau\|_{\text{SO}(3)} + \|\nabla\tau\|_{\text{SO}(3)}^2. \quad (\text{C.22})$$

Then consider the reduction term

$$h\left(r_{\rho_r}^{z^{-1}}(r_{u_r}^{-1}(u))\right) \sin(\theta_r) - h\left(r_{\rho_r}^{z^{-1}}(r_{\tau^*(u_r)}^{-1}(u))\right) \sin(\theta_r + \tau^{*\theta}(\theta_r, \phi_r))$$

which can be divided into two sub-terms as

$$\begin{aligned} &\sin(\theta_r) \left[h\left(r_{\rho_r}^{z^{-1}}(r_{u_r}^{-1}(u))\right) - h\left(r_{\rho_r}^{z^{-1}}(r_{\tau^*(u_r)}^{-1}(u))\right) \right] \\ &+ h\left(r_{\rho_r}^{z^{-1}}(r_{\tau^*(u_r)}^{-1}(u))\right) [\sin(\theta_r) - \sin(\theta_r + \tau^{*\theta}(\theta_r, \phi_r))]. \end{aligned} \quad (\text{C.23})$$

For the first term in (C.23), it is determined by two points $r_{\rho_r}^{z^{-1}}(r_{u_r}^{-1}(u))$ and $r_{\rho_r}^{z^{-1}}(r_{\tau^*(u_r)}^{-1}(u))$. We start by considering two points $r_{\tau^*(u_r)}^{-1}(u)$ and $r_{u_r}^{-1}(u)$. Due to the symmetry of the sphere, we can alternatively consider two points $r_{\tau^*(u_r)}(u)$ and $r_{u_r}(u)$ such that

$$r_{\tau^*(u_r)}(u) = r_{\tau^*(u_r)}\left(r_{u_r}^{-1}(r_{u_r}(u))\right) = \tau_{u_r}^*(r_{u_r}(u)) \quad (\text{C.24})$$

where $\tau_{u_r}^* = r_{\tau^*(u_r)} \circ r_{u_r}^{-1}$ is the local rotation of τ^* at the point u_r [cf. (19)], whose rotation angle is bounded by $\|\tau\|_{\text{SO}(3)}$ [cf. (25)]. The shortest arc connecting these two points on the sphere is then bounded by

$$\text{arc}(r_{u_r}(u), r_{\tau^*(u_r)}(u)) \leq \|\tau\|_{\text{SO}(3)}, \quad \forall u \in \mathbb{S}_2 \quad (\text{C.25})$$

since points are defined on the unit sphere. Thus, due to the symmetry of the sphere, we have $\text{arc}(r_{u_r}^{-1}(u), r_{\tau^*(u_r)}^{-1}(u)) \leq \|\tau\|_{\text{SO}(3)}$ for all $u \in \mathbb{S}_2$. Since $r_{\rho_r}^{z-1}$ is the rotation along z -axis that does not change the distance between two points on the sphere, we get

$$\text{arc}\left(r_{\rho_r}^{z-1}(r_{u_r}^{-1}(u)), r_{\rho_r}^{z-1}(r_{\tau^*(u_r)}^{-1}(u))\right) \leq \|\tau\|_{\text{SO}(3)}, \quad \forall u \in \mathbb{S}_2. \quad (\text{C.26})$$

With the Lipschitz property of filter h , we get

$$\begin{aligned} & \left| \sin(\theta_r) \left[h(r_{u_r}^{-1}(u)) - h(r_{\tau^*(u_r)}^{-1}(u)) \right] \right| \\ & \leq C_h \text{arc}\left(r_{\rho_r}^{z-1}(r_{\phi_r \theta_r \rho_r}^{-1}(u)), r_{\rho_r}^{z-1}(r_{\tau^*(u_r)}^{-1}(u))\right) \leq C_h \|\tau\|_{\text{SO}(3)}. \end{aligned} \quad (\text{C.27})$$

For the second term in (C.23), by using the truncated Taylor Expansion, we can represent $\sin(\theta_r + \tau^{*\theta}(\theta_r, \phi_r))$ as

$$\sin(\theta_r + \tau^{*\theta}(\theta_r, \phi_r)) = \sin(\theta_r) + \cos(\theta_r + t\tau^{*\theta}(\theta_r, \phi_r))\tau^{*\theta}(\theta_r, \phi_r) \quad (\text{C.28})$$

with some $t \in (0, 1)$. Now denote by $u_1 = u_r = (\theta_r, \phi_r)$ and $u_2 = \tau^*(u_1) = (\theta_r + \tau^{*\theta}(\theta_r, \phi_r), \phi_r + \tau^{*\phi}(\theta_r, \phi_r))$ two points on the sphere, and consider the triangle $\Delta u_1 u_0 u_2$ with $u_0 = (0, 0)$. Since the difference between two sides is less than the third side, we have $|\overline{u_0 u_1} - \overline{u_0 u_2}| \leq \overline{u_1 u_2}$. Therefore, we get

$$|\text{arc}(u_0, u_1) - \text{arc}(u_0, u_2)| \leq \text{arc}(u_1, u_2). \quad (\text{C.29})$$

Also since $u_2 = \tau^*(u_1) = \tau_{u_1}^*(u_1)$ where $\tau_{u_1}^*$ is the local rotation of τ^* at the point u_1 and $\text{arc}(u_1, u_2)$ is the shortest distance between u_1 and u_2 , we have $\text{arc}(u_1, u_2) \leq \|\tau\|_{\text{SO}(3)}$. By using this result in (C.29) and the facts that $\text{arc}(u_0, u_1) = \theta_r$ and $\text{arc}(u_0, u_2) = \theta_r + \tau^{*\theta}(\theta_r, \phi_r)$ in the unit sphere, we have

$$|\theta_r + \tau^{*\theta}(\theta_r, \phi_r) - \theta_r| = |\tau^{*\theta}(\theta_r, \phi_r)| \leq \|\tau\|_{\text{SO}(3)}. \quad (\text{C.30})$$

By substituting (C.30) into (C.28) and the latter into the second term in (C.23) together with the fact that $|\cos(\theta_r + t\tau^{*\theta}(\theta_r, \phi_r))| \leq 1$, we get

$$\left| h\left(r_{\rho_r}^{z-1}(r_{\tau^*(u_r)}^{-1}(u))\right) [\sin(\theta) - \sin(\theta_r + \tau^{*\theta}(\theta_r, \phi_r))] \right| \leq C_h \|\tau\|_{\text{SO}(3)}. \quad (\text{C.31})$$

Further substituting (C.22), (C.27) and (C.31) into $k_2(\theta_r, \phi_r, \rho_r, \theta_u, \phi_u)$ yields

$$\begin{aligned} & |k_2(\theta_r, \phi_r, \rho_r, \theta_u, \phi_u)| \\ & \leq 2C_h \|\tau\|_{\text{SO}(3)} \left(1 + 2\|\nabla\tau\|_{\text{SO}(3)} + \|\nabla\tau\|_{\text{SO}(3)}^2\right) \leq 2C_h\epsilon + \mathcal{O}(\epsilon^2) \end{aligned} \quad (\text{C.32})$$

where $\|\tau\|_{\text{SO}(3)} \leq \epsilon$ and $\|\nabla\tau\|_{\text{SO}(3)} \leq \epsilon$ are used in the last inequality.

By using (C.21) and (C.32), we bound the operator $k(\theta_r, \phi_r, \rho_r, \theta_u, \phi_u)$ as

$$|k(\theta_r, \phi_r, \rho_r, \theta_u, \phi_u)| \leq 4C_h\epsilon + \mathcal{O}(\epsilon^2). \quad (\text{C.33})$$

Therefore, we obtain

$$\frac{1}{8\pi^2} \int |k(\theta_r, \phi_r, \rho_r, \theta_u, \phi_u)| d\theta_r d\phi_r d\rho_r \leq 4C_h\epsilon + \mathcal{O}(\epsilon^2), \quad (\text{C.34})$$

$$\frac{1}{2\pi^2} \int |k(\theta_r, \phi_r, \rho_r, \theta_u, \phi_u)| d\theta_u d\phi_u \leq 4C_h\epsilon + \mathcal{O}(\epsilon^2). \quad (\text{C.35})$$

Then by using the Schur's Lemma, we have

$$\|H - HP_\tau^{*-1}\| \leq 4C_h\epsilon + \mathcal{O}(\epsilon^2). \quad (\text{C.36})$$

Finally, by substituting (C.8) and (C.36) into (C.5) and the latter into (C.3), we complete the proof

$$\|H(x_\tau) - H(x)\|_{\text{SO}(3)} \leq \|HP_\tau^* - H\| \|\mathbf{x}\| \leq 8C_h\epsilon \|\mathbf{x}\| + \mathcal{O}(\epsilon^2). \quad (\text{C.37})$$

□

Appendix D. Proof of Proposition 2

Proof of Proposition 2. Without loss of generality, we consider multi-feature Spherical CNN. From Proposition 1, we know that the rotation equivariance holds for spherical convolutional filters. Then at layer ℓ of the SCNN, each filter h_ℓ^{fg} satisfies

$$H_\ell^{fg} \left((x_{(\ell-1)}^g)_r \right) = \left(H_\ell^{fg}(x_{\ell-1}^g) \right)_r, \quad \forall f = 1, \dots, F_\ell, \quad g = 1, \dots, F_{\ell-1}, \quad (\text{D.1})$$

where $(x_{\ell-1}^g)_r$, $(H_\ell^{fg}(x_{\ell-1}^g))_r$ are rotated signals of $x_{\ell-1}^g$, $H_\ell^{fg}(x_{\ell-1}^g)$ by r . Since linear operations does not break the rotation equivariance, we have

$$\sum_{g=1}^F H_\ell^{fg} \left((x_{\ell-1}^g)_r \right) = \left(\sum_{g=1}^F H_\ell^{fg}(x_{\ell-1}^g) \right)_r. \quad (\text{D.2})$$

Note that the pointwise nonlinearity $\sigma(\cdot)$ applies to each element of the spherical signal x such that we have $\sigma(x_r) = (\sigma(x))_r$. Thus, we can further get

$$\sigma \left(\sum_{g=1}^F H_\ell^{fg} \left((x_{\ell-1}^g)_r \right) \right) = \left(\sigma \left(\sum_{g=1}^F H_\ell^{fg}(x_{\ell-1}^g) \right) \right)_r. \quad (\text{D.3})$$

Since (D.3) holds at each layer $\ell = 1, \dots, L$, we conclude that the rotation equivariance holds for the Spherical CNN. \square

Appendix E. Proof of Theorem 2

We need the following lemma that shows the propagation consequence of a spherical signal through the spherical convolutional filter.

Lemma 1. *Let $x \in \mathbb{L}^2(\mathbb{S}_2)$ be a spherical signal, and H be a Lipschitz spherical convolutional filter with respect to C_h [cf. Def 4]. Then, it holds that*

$$\|H(x)\| \leq C_h \|x\|. \quad (\text{E.1})$$

Proof. The output of the spherical convolutional filter is [cf. (7)]

$$\begin{aligned} H(x)(u) &= \frac{1}{8\pi^2} \int h(r_{\phi_r, \theta_r, \rho_r}^{-1}(u)) x(\theta_r, \phi_r) \sin(\theta_r) d\theta_r d\phi_r d\rho_r \\ &= \frac{1}{8\pi^2} \int k(\theta_r, \phi_r, \rho_r, \theta_u, \phi_u) x(\theta_r, \phi_r) d\theta_r d\phi_r d\rho_r \end{aligned} \quad (\text{E.2})$$

where $r_{\phi_r, \theta_r, \rho_r}^{-1}$ is the inverse rotation characterized by the Euler angles $(\phi_r, \theta_r, \rho_r)$ and $k(\theta_r, \phi_r, \rho_r, \theta_u, \phi_u)$ is the operation kernel. Since $|h(\theta_r, \phi_r)| \leq C_h$, we have

$$\frac{1}{8\pi^2} \int |k(\theta_r, \phi_r, \rho_r, \theta_u, \phi_u)| d\theta_r d\phi_r d\rho_r \leq C_h, \quad \frac{1}{2\pi^2} \int |k(\theta_r, \phi_r, \rho_r, \theta_u, \phi_u)| d\theta_u d\phi_u \leq C_h$$

By using the Schur's Lemma in (C.17) and (C.18), we complete the proof $\|H(x)\| \leq C_h \|x\|$. \square

Proof. The output of the Spherical CNN is $\Phi(x; \mathcal{H}) = \sigma_L(\sum_{f=1}^F h_L^f *_{\text{SO}(3)} x_{L-1}^f)$. Denote by $H_L^f x_{L-1}^f = h_L^f *_{\text{SO}(3)} x_{L-1}^f$ and $P_\tau x = x_\tau$ concise notions of the spherical convolution and the perturbed signal. The output difference induced by τ is

$$\begin{aligned} \|\Phi(P_\tau x; \mathcal{H}) - \Phi(x; \mathcal{H})\| &= \left\| \sigma\left(\sum_{f=1}^F H_L^f \hat{x}_{L-1}^f\right) - \sigma\left(\sum_{f=1}^F H_L^f x_{L-1}^f\right) \right\| \\ &\leq C_\sigma \left\| \sum_{f=1}^F H_L^f \hat{x}_{L-1}^f - \sum_{f=1}^F H_L^f x_{L-1}^f \right\| \end{aligned} \quad (\text{E.3})$$

where \hat{x}_{L-1}^f and x_{L-1}^f are the f th outputs of $\Phi(P_\tau x; \mathcal{H})$ and $\Phi(x; \mathcal{H})$ at $(L-1)$ th layer, respectively. The last inequality is due to the Lipschitz property of the nonlinearity $\sigma(\cdot)$. Since the spherical convolutional filter is linear, we get

$$\|\Phi(P_\tau x; \mathcal{H}) - \Phi(x; \mathcal{H})\| \leq \sum_{f=1}^F C_\sigma \|H_L^f (\hat{x}_{L-1}^f - x_{L-1}^f)\| \leq C_\sigma C_h \sum_{f=1}^F \|\hat{x}_{L-1}^f - x_{L-1}^f\| \quad (\text{E.4})$$

where the first inequality is due to the triangle inequality and the second is obtained from Lemma 1. We observe a recursive process in (E.4) that the output difference at L th layer is upper bounded by that at $(L-1)$ th layer. By repeating this process, we have $\|\hat{x}_{L-1}^f - x_{L-1}^f\| \leq C_\sigma C_h \sum_{g=1}^F \|\hat{x}_{L-2}^g - x_{L-2}^g\|$. Substituting this result into (E.4) yields

$$\|\Phi(P_\tau x; \mathcal{H}) - \Phi(x; \mathcal{H})\| \leq C_\sigma^2 C_h^2 F \sum_{g=1}^F \|\hat{x}_{L-2}^g - x_{L-2}^g\|. \quad (\text{E.5})$$

By doing this recursively, we have

$$\|\Phi(P_\tau x; \mathcal{H}) - \Phi(x; \mathcal{H})\| \leq C_\sigma^{L-1} C_h^{L-1} F^{L-2} \sum_{g=1}^F \|\hat{x}_1^g - x_1^g\| \quad (\text{E.6})$$

where \hat{x}_1^g and x_1^g are the g th outputs of $\Phi(P_\tau x; \mathcal{H})$ and $\Phi(x; \mathcal{H})$ at 1st layer.

Now consider the term $\|\hat{x}_1^g - x_1^g\|$, which is given by the definition as

$$\|\hat{x}_1^g - x_1^g\| = \|\sigma(H_1^g P_\tau x) - \sigma(H_1^g x)\| \leq C_\sigma \|H_1^g P_\tau x - H_1^g x\| \quad (\text{E.7})$$

where x is the input signal and the last inequality is due to the Lipschitz property of the nonlinearity. From Theorem 1, under the rotation distance we have

$$\|H_1^g P_\tau x - H_1^g x\|_{\text{SO}(3)} \leq 8C_h \epsilon \|x\| + \mathcal{O}(\epsilon^2). \quad (\text{E.8})$$

Note that (E.8) holds for any filters $\{h_1^g\}_{g=1}^F$ at 1st layer. By substituting (E.8) into (E.7), we get $\|\hat{x}_1^g - x_1^g\|_{\text{SO}(3)} \leq 8C_h C_\sigma \epsilon \|x\| + \mathcal{O}(\epsilon^2)$ for all $g = 1, \dots, F$. By further substituting this result into (E.6), we complete the proof

$$\|\Phi(P_\tau x; \mathcal{H}) - \Phi(x; \mathcal{H})\|_{\text{SO}(3)} \leq 8C_h^L C_\sigma^L F^{L-1} \epsilon \|x\| + \mathcal{O}(\epsilon^2). \quad (\text{E.9})$$

□

References

- [1] S. E. Reutebuch, H. Andersen, R. J. McGaughey, Light detection and ranging (lidar): an emerging tool for multiple resource inventory, *Journal of forestry* 103 (6) (2005) 286–292.
- [2] A. Chang, A. Dai, T. Funkhouser, M. Halber, M. Niebner, M. Savva, S. Song, A. Zeng, Y. Zhang, Matterport3d: Learning from rgb-d data in indoor environments, in: 5th International Conference on 3D Vision, Qingdao, China, 2017, pp. 667–676.
- [3] M. R. Dury, S. D. Woodward, S. B. Brown, M. B. McCarthy, Surface finish and 3d optical scanner measurement performance for precision engineering, in: 30th Annual Meeting of the American Society for Precision Engineering, ASPE, Austin, TX, 2015, pp. 1–6.
- [4] K. Zhou, H. Bao, J. Shi, 3d surface filtering using spherical harmonics, *Computer-Aided Design* 36 (4) (2004) 363–375.
- [5] F. J. Simons, A. Plattner, Scalar and vector slepian functions, spherical signal estimation and spectral analysis, arXiv preprint arXiv:1306.3184 [physics.data-an].
URL <https://arxiv.org/abs/1306.3184>
- [6] E. Racah, C. Beckham, T. Maharaj, S. E. Kahou, M. Prabhat, C. Pal, Extremeweather: A large-scale climate dataset for semi-supervised detection,

- localization, and understanding of extreme weather events, in: 31st Conference on Neural Information Processing Systems, Neural Inform. Process. Foundation, Long Beach, CA, 2017, pp. 3402–3413.
- [7] M. Yavartanoo, E. Y. Kim, K. M. Lee, Spnet: Deep 3d object classification and retrieval using stereographic projection, in: 14th Asian Conference on Computer Vision, Springer, Perth, Australia, 2018, pp. 691–706.
 - [8] A. Geiger, P. Lenz, C. Stiller, R. Urtasun, Vision meets robotics: The kitti dataset, *The International Journal of Robotics Research* 32 (11) (2013) 1231–1237.
 - [9] L. Maier-Hein, P. Mountney, A. Bartoli, et al., Optical techniques for 3d surface reconstruction in computer-assisted laparoscopic surgery, *Medical image analysis* 17 (8) (2013) 974–996.
 - [10] A. Makadia, L. Sorgi, K. Daniilidis, Rotation estimation from spherical images, in: 17th International Conference on Pattern Recognition, IEEE, Cambridge, UK, 2004, pp. 590–593.
 - [11] A. Makadia, K. Daniilidis, Rotation recovery from spherical images without correspondences, *IEEE transactions on pattern analysis and machine intelligence* 28 (7) (2006) 1170–1175.
 - [12] I. M. Gelfand, R. A. Minlos, Z. Y. Shapiro, Representations of the Rotation and Lorentz Groups and their Applications, Courier Dover Publications, 2018.
 - [13] A. Derighetti, Convolution operators on groups, Springer, 2011.
 - [14] A. Makadia, K. Daniilidis, Spherical correlation of visual representations for 3d model retrieval, *International Journal of Computer Vision* 89 (2-3) (2010) 193–210.
 - [15] Y. Su, K. Grauman, Learning spherical convolution for fast features from 360 imagery, in: 31st Conference on Neural Information Processing Sys-

- tems, Neural Inform. Process. Foundation, Long Beach, CA, 2017, pp. 529–539.
- [16] C. Esteves, C. Allen-Blanchette, A. Makadia, K. Daniilidis, Learning $so(3)$ equivariant representations with spherical cnns, in: European Conference on Computer Vision, Munich, Germany, 2018, pp. 52–68.
 - [17] T. S. Cohen, M. Geiger, J. Khler, M. Welling, Spherical cnns, in: 6th International Conference on Learning Representations, Vancouver, BC, 2018.
 - [18] D. E. Worrall, S. J. Garbin, D. Turmukhambetov, G. J. Brostow, Harmonic networks: Deep translation and rotation equivariance, in: 30th Conference on Computer Vision and Pattern Recognition, IEEE, Hawaii, HO, 2017, pp. 5028–5037.
 - [19] B. S. Veeling, J. Linmans, J. Winkens, T. Cohen, M. Welling, Rotation equivariant cnns for digital pathology, in: 21st International Conference on Medical image computing and computer-assisted intervention, Granada, Spain, 2018, pp. 210–218.
 - [20] J. Li, Y. Bi, G. H. Lee, Discrete rotation equivariance for point cloud recognition, in: International Conference on Robotics and Automation, IEEE, Montreal, Canada, 2019, pp. 7269–7275.
 - [21] R. Khasanova, P. Frossard, Graph-based isometry invariant representation learning, in: International Conference on Machine Learning, PMLR, Sydney, Australia, 2017, pp. 1847–1856.
 - [22] P. Frossard, R. Khasanova, Graph-based classification of omnidirectional images, in: International Conference on Computer Vision Workshops, IEEE, Venice, Italy, 2017, pp. 860–869.
 - [23] N. Perraudin, M. Defferrard, T. Kacprzak, R. Sgier, Deepsphere: Efficient spherical convolutional neural network with healpix sampling for cosmological applications, *Astronomy and Computing* 27 (2019) 130–146.

- [24] M. Defferrard, M. Milani, F. Gusset, N. Perraudin, Deepsphere: a graph-based spherical cnn, arXiv preprint arXiv:2012.15000 [cs.LG].
URL <https://arxiv.org/abs/2012.15000>
- [25] Z. Wu, S. Song, A. Khosla, F. Yu, L. Zhang, X. Tang, J. Xiao, 3d shapenets: A deep representation for volumetric shapes, in: 28th Conference on Computer Vision and Pattern Recognition, IEEE, Boston, MA, 2015, pp. 1912–1920.
- [26] J. E. Mebius, Derivation of the euler-rodrigues formula for three-dimensional rotations from the general formula for four-dimensional rotations, arXiv preprint arXiv:math/0701759 [math.GM].
URL <https://arxiv.org/abs/math/0701759>
- [27] W. R. Scott, Group theory, Courier Corporation, 2012.
- [28] P. J. Kostelec, D. N. Rockmore, Ffts on the rotation group, Journal of Fourier analysis and applications 14 (2) (2008) 145–179.
- [29] J. R. Driscoll, D. M. Healy, Computing fourier transforms and convolutions on the 2-sphere, Advances in applied mathematics 15 (2) (1994) 202–250.
- [30] S. Mallat, Group invariant scattering, Communications on Pure and Applied Mathematics. 65 (10) (2012) 1331–1398.
- [31] I. Goodfellow, Y. Bengio, A. Courville, Deep Learning, Adaptive Computation Mach. Learning Series, The MIT Press, Cambridge, MA, 2016.
- [32] A. Krizhevsky, I. Sutskever, G. E. Hinton, Imagenet classification with deep convolutional neural networks, in: 26th Conference on Neural Information Processing Systems, Neural Inform. Process. Foundation, Harrahs and Harveys, Lake Tahoe, 2012, pp. 1097–1105.
- [33] B. Hu, Z. Lu, H. Li, Q. Chen, Convolutional neural network architectures for matching natural language sentences, in: 28th Conference on Neural Information Processing Systems, Neural Inform. Process. Foundation, Montreal, CANADA, 2014, pp. 2042–2050.

- [34] H. Li, Z. Lin, X. Shen, J. Brandt, G. Hua, A convolutional neural network cascade for face detection, in: 28th Conference on Computer Vision and Pattern Recognition, IEEE, Boston, MA, 2015, pp. 5325–5334.
- [35] J. Bruna, W. Zaremba, A. Szlam, Y. LeCun, Spectral networks and deep locally connected networks on graphs, in: 2nd International Conference on Learning Representations, Banff, AB, 2014, pp. 1–14.
- [36] M. Defferrard, X. Bresson, P. Vandergheynst, Convolutional neural networks on graphs with fast localized spectral filtering, in: 30th Conference on Neural Information Processing Systems, Neural Inform. Process. Foundation, Barcelona, Spain, 2016, pp. 3844–3858.
- [37] F. Gama, A. G. Marques, G. Leus, A. Ribeiro, Convolutional neural network architectures for signals supported on graphs, *IEEE Transactions on Signal Processing* 67 (4) (2019) 1034–1049.
- [38] F. Gama, J. Bruna, A. Ribeiro, Stability properties of graph neural networks, *IEEE Transactions on Signal Processing* 68 (2020) 5680–5695.
- [39] K. Chen, L. Liu, Geometric data perturbation for privacy preserving outsourced data mining, *Knowledge and information systems* 29 (3) (2011) 657–695.
- [40] W. Huang, R. Wang, Y. Chen, H. Li, S. Gan, Damped multichannel singular spectrum analysis for 3d random noise attenuation, *Geophysics* 81 (4) (2016) V261–V270.
- [41] M. A. Nazari S., S. Gholtashi, A. R. Kahoo, W. Chen, Y. Chen, Data-driven multitask sparse dictionary learning for noise attenuation of 3d seismic data, *Geophysics* 82 (6) (2017) V385–V396.
- [42] J. Schur, Bemerkungen zur theorie der beschränkten bilinearformen mit unendlich vielen veränderlichen., *Journal für die reine und angewandte Mathematik (Crelles Journal)* 1911 (140) (1911) 1–28.